



HAL
open science

Optical and Electrochemical Properties of Self-Organized TiO₂ Nanotube Arrays from Anodized Ti-6Al-4V Alloy

Henia Fraoucene, Vinsensia Ade Sugiawati, Djedjiga Hatem, Mohamed Said Belkaid, Florence Vacandio, Marielle Eyraud, Marcel Pasquinelli, Thierry Djenizian

► **To cite this version:**

Henia Fraoucene, Vinsensia Ade Sugiawati, Djedjiga Hatem, Mohamed Said Belkaid, Florence Vacandio, et al.. Optical and Electrochemical Properties of Self-Organized TiO₂ Nanotube Arrays from Anodized Ti-6Al-4V Alloy. *Frontiers in Chemistry*, 2019, 7, 10.3389/fchem.2019.00066 . hal-02461562

HAL Id: hal-02461562

<https://hal.science/hal-02461562v1>

Submitted on 6 Feb 2020

HAL is a multi-disciplinary open access archive for the deposit and dissemination of scientific research documents, whether they are published or not. The documents may come from teaching and research institutions in France or abroad, or from public or private research centers.

L'archive ouverte pluridisciplinaire **HAL**, est destinée au dépôt et à la diffusion de documents scientifiques de niveau recherche, publiés ou non, émanant des établissements d'enseignement et de recherche français ou étrangers, des laboratoires publics ou privés.

Optical and Electrochemical Properties of Self-Organized TiO₂ Nanotube Arrays from Anodized Ti-6Al-4V Alloy

Henia Fraoucene¹, Vinsensia Ade Sugiawati², Djedjiga Hatem¹, Mohammed Said Belkaid¹, Florence Vacandio^{2*}, Marielle Eyraud², Marcel Pasquinelli³ and Thierry Djenizian⁴

¹Laboratory of Advanced Technologies of Genie Electrics (LATAGE), Faculty of Electrical and Computer Engineering Mouloud Mammeri University (UMMTO), Tizi-Ouzou, Algeria

² Aix-Marseille Université, CNRS, Electrochemistry of Materials Research Group, MADIREL, UMR 7246, F-13397, Marseille Cedex 20, France

³Institute of Microelectronic Materials Nanosciences of Provence (IM2NP), Optoelectronics and photovoltaics (OPTO-PV) team, University of Provence, St Jérôme Center, Marseille, France

⁴Mines Saint-Etienne, Center of Microelectronics in Provence, Department of Flexible Electronics, F – 13541 Gardanne, France

*Correspondence:

FlorenceVacandio

florence.vacandio@univ-amu.fr

Abstract

Due to their high specific surface area and advanced properties, TiO₂ nanotubes (TiO₂ NTs) have a great significance for production and storage of energy. In this paper, TiO₂ NTs were synthesized from anodization of Ti-6Al-4V alloy at 60 V for 3 hours in fluoride ethylene glycol electrolyte by varying the water content and further annealing treatment. The morphological, structural, optical and electrochemical performances of TiO₂ NTs were investigated by scanning electron microscope (SEM), energy dispersive X-ray spectroscopy (EDS), X-ray diffraction (XRD), UV-Visible spectroscopy and electrochemical characterization techniques. By varying the water content in the solution, a honeycomb and porous structure was obtained at low water content and the presence of ($\alpha + \beta$) phase in Ti-6Al-4V alloy caused not uniform etching. With an additional increase in water content, a nanotubular structure is formed in the ($\alpha + \beta$) phases with different morphological parameters. The anatase TiO₂ NTs synthesized with 20 wt% H₂O shows an improvement in absorption band that extends into the visible region due the presence of vanadium oxide in the structure and the effective band gap energy (E_g) value of 2.25 eV. The TiO₂ NTs electrode also shows a good cycling performance, delivering a reversible capacity of 82 mAh.g⁻¹ (34 μ Ah.cm⁻². μ m⁻¹) at 1C rate over 50 cycles.

Keywords: TiO₂ nanotubes, Ti-6Al-4V alloy, anodization, Li-ion microbatteries, negative electrode.

1. Introduction

Rechargeable batteries play an important role in powering the electronic devices and in storing energy due to their high energy and power density which are expected to be a solution

44 for the future energy storage requirements (Liet al., 2017). Due to the lack of suitable on-
45 board power sources, the advances in the miniaturization of microelectronics is growing,
46 opening opportunities to explore the both cathode and anode materials as thin-films
47 (Sugiawati et al., 2016) and nanostructured electrodes by utilizing various synthesis and
48 deposition techniques (Sugiawati et al., 2018; Xiong et al., 2014; Djenizian et al., 2011; Pikul
49 et al., 2013; Ellis et al., 2014).

50 Titanium dioxide (TiO₂) is a semiconductor material that has been studied extensively in the
51 last few decades due to its chemical stability, non-toxicity and biocompatibility (Morozová et
52 al., 2012; Reszczyńska et al., 2014; Pansila et al., 2012). In Li-ion microbatteries, the
53 electrochemical performances of anode materials are highly dependent on their morphologies,
54 surface characteristics, and particle sizes. Many researchers proposed to reduce the size of
55 TiO₂ anode material to the nanometer scale in order to increase not only the number of
56 reaction sites, but also gives new properties to the materials (Armstrong et al., 2005). Among
57 these nanostructured materials, self-organized TiO₂ nanotubes (TiO₂ NTs) obtained by
58 anodization of Ti foil can give a high porosity and larger specific area offering an
59 enhancement in the cell capacity and cycle life (Kyeremateng et al., 2013b; Panda et al., 2012;
60 Fang et al., 2009; Chang et al., 2015; Ortiz et al., 2008, 2009; Salian et al., 2017; Plylahan et
61 al., 2014).

62 In addition, physical and electrochemical performance of TiO₂ NTs can be enhanced by
63 chemical modification of the surface (Kyeremateng et al., 2013a; Sopha et al., 2017; Plylahan
64 et al., 2012) and by incorporation of foreign ions into TiO₂ lattice such as Sn⁴⁺ (Kyeremateng
65 et al., 2013b), Fe³⁺ (Das et al., 2011), Ni²⁺ (Choi et al., 2009), Nb⁵⁺ (Salian et al., 2018) and
66 V³⁺ (Lin et al., 2013). The electrical conductivity and electrochemical kinetics of TiO₂ NTs
67 electrodes can be improved by doping with Ti³⁺ ions due to a Li⁺ diffusion coefficient of 1.09
68 x 10⁻¹² cm² s⁻¹ which is almost one order of magnitude higher than that of TiO₂ NTs (1.39 x
69 10⁻¹³ cm² s⁻¹) (Duan et al., 2016). Yu et al. also demonstrated that 5 at.% Sn doped TiO₂ NTs
70 exhibits the best cycling stability with specific capacity of 386 mAh.g⁻¹ and coulombic
71 efficiency of 99.2 % after 50 cycles at 0.1C (Yu et al., 2014).

72 Ternary titanium alloy (Ti-6Al-4V, with 6 wt% Aluminium and 4 wt% Vanadium) have also
73 been utilized to synthesize the self-organized TiO₂ NTs, notably for their use in a wide range
74 of applications such as bone substitute applications, including orthopedic and dental implants
75 due to their superior compatibility, mechanical resistance, excellent corrosion resistance, and
76 good thermal stability (Long and Rack, 1998; Black and Hastings, 2013). Furthermore,
77 research works focused to improve the osseointegration and stability of the TA6V implant in
78 the human body (Jo et al., 2013). However, to the best of our knowledge, there have been no
79 reports to date on the use of the anodized TA6V alloy as electrode for Li-ion microbatteries.
80 The basic objective of this work is therefore to study the electrochemical performance and
81 optical properties of the anodized TA6V alloy produced through electrochemical anodization
82 in fluoride-containing ethylene glycol electrolyte.

83

84 **2. Experimental**

85 **2.1. Synthesis of TiO₂ nanotubes**

86 The Ti-6Al-4V (TA6V) alloy (0.1 mm thickness, 25% tolerance, Goodfellow) were cut into
87 square shape (1.2 cm x 1.2 cm) with a selected work area of 0.6 cm². Before anodization, the
88 Ti-6Al-4V foils were degreased by sonication in acetone, 2-propanol and methanol for 10

89 min each, rinsed with ultrapure water and dried in a stream of compressed air. The
90 anodization was performed in a two-electrode electrochemical cell with Ti–6Al–4V foil as the
91 anode and platinum foil as the cathode. At room temperature, all anodization experiments
92 were carried out under a constant voltage of 60 V using a generator (ISO-TECH IPS-603) for
93 3 hours. Ethylene glycol (EG) solution containing 0.3 wt% ammonium fluoride (NH₄F) was
94 used as electrolyte, and the water content was varied at 2, 5, 10,15, and 20 wt%. After
95 anodization, the samples were soaked in ultrapure water for 10 min and then dried in an oven
96 at 50 °C for 10 min. In order to transform the amorphous crystallographic structure obtained
97 just after electrochemical anodization into crystalline structure, the samples were annealed at
98 500 °C for 3 hours with a heating and cooling rate of 5 °C/min.

99 **2.2. Characterization of the samples**

100 Morphological characterization of the TiO₂ NTs was investigated by scanning electron
101 microscopy (SEM) using a PHILIPS XL30. The chemical composition was analyzed by
102 energy dispersive X-ray spectroscopy (EDS). The crystalline phases were characterized by X-
103 ray diffraction (XRD) analysis. The diffraction patterns were obtained by a X'Pert Philips
104 MPD with a Panalytical X'Celerator detector using a graphite monochromized CuK α
105 radiation ($\lambda=1.5418\text{\AA}$). The measurements were performed within the range of 2θ from 20°
106 to 70°. The optical properties were investigated using a UV-Visible spectroscopy from 250 to
107 800 nm.

108 The electrochemical performance tests were performed using two-electrode Swagelok cells
109 assembled in an argon-filled glove box in which the oxygen and moisture contents were less
110 than 2 ppm. A 9 mm diameter Li foil was used as the counter electrode and two sheets of
111 Whatman glass microfiber separator were soaked in the electrolyte of lithium
112 hexafluorophosphate in ethylene carbonate and diethylene carbonate electrolyte (1M LiPF₆ in
113 EC/DEC of 1:1 w/w) purchased from Sigma-Aldrich prior to assembling the cell. The cycling
114 experiments were performed using a VMP3 potentiostat-galvanostat (Biologic, France). For
115 all experiments, no additives such as poly (vinyl difluoride) as binder and carbon black as
116 conductive agent were utilized. Cyclic voltammetry (CV) measurements were performed in
117 the range voltage of 1-3 V vs. Li/Li⁺ at a scan rate of 0.05, 0.1 and 0.5 mV.s⁻¹, respectively.
118 For galvanostatic discharge–charge tests, a constant current density of 3.23 $\mu\text{A.cm}^{-2}$ (C/10),
119 6.47 $\mu\text{A.cm}^{-2}$ (C/5), 16.18 $\mu\text{A.cm}^{-2}$ (C/2), and 32.35 $\mu\text{A.cm}^{-2}$ (1C), respectively, was
120 applied to the assembled cells with a cut-off potential of 1- 3 V vs. Li/Li⁺.

121

122 **3. Experimental Results**

123 **3.1. Morphological and chemical characterization**

124 **Surface Morphology**

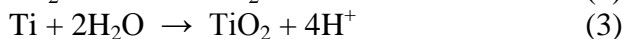
125 Figure 1 shows the SEM images of the different morphologies of TA6V alloy anodized at 60
126 V for 3 hours in Ethylene Glycol (EG) solution containing 0.3 wt% NH₄F with different water
127 contents. It should be noticed that the ternary titanium alloy studied in the present work
128 consist of two metallurgical phases, the α phase being enriched in Al and the β phase in V
129 (Macak et al., 2005). We noted a great influence of the water content on the formation of the
130 self-organized TiO₂ NTs, both randomly arranged porous structure and uniformly arranged
131 nanotubes. The formation of the porous structure depends on the underlying phase (α or β)
132 and the anodization parameters. As seen in Figure 1a, a honeycomb is obviously formed on the
133 surface at water content of 2 wt%, however not on the entire surface. Figure 1b-d exhibits the
134 positive influence of the improved water content, from 5 to 15 wt%. The β phase is
135 preferentially etched as the amount of water in the solution increases, indicating the enhanced

136 solubility of the vanadium oxides. A similar phenomenon has been previously reported for the
 137 TiO₂ NTs grown from anodization of TA6V alloy in different electrolytes
 138 (sulphuric/hydrofluoric acid and ammonium sulphate with 0.2 wt% NH₄F, respectively) at
 139 controlled voltage and anodization time (Matykina et al., 2011; Moravec et al., 2016).
 140 According to Figure 1e and f, a well-separated TiO₂ NTs with an inner diameter varying
 141 between 97 to 206 nm and a length of 1.25 μm can be formed in the fluoride-containing EG
 142 electrolyte carrying 20 wt% H₂O. At this percentage, the nanotubular structure is formed in
 143 the two phases (α + β) via the formation of an oxide layer (TiO₂) and the chemical dissolution
 144 of this layer assisted by an electric field. The formation mechanism of TiO₂ NTs from alloys
 145 is similar to that of the pristine TiO₂ NTs obtained from anodization of pure Ti..

146
147
148
149
150 **Figure 1.**

151
152
153
154
155 **Composition Analysis**

156
157 Figure 2 shows the EDS spectra of TiO₂ NTs grown from anodization of TA6V alloy with 20
 158 wt% H₂O content in the fluoride EG. The energy dispersive X-ray characterization values are
 159 summarized in Table I. After anodization, there is a slight difference of wt% for each element
 160 and the strong presence of oxygen confirming the formation of oxides. In fact, the wt% of Ti
 161 in the anodized TA6V alloy is lower compared to that of the pristine TA6V alloy. This result
 162 suggests that Ti anode is oxidized into TiO₂ through the oxidation of Ti to form Ti⁴⁺
 163 according to Equation (1).



168
169 The reduction of H₂O takes place at the cathode (Equation 2) and the overall reaction known
 170 as hydrolysis reaction leads to the formation of the titanium dioxide (Equation 3). TiO₂ NTs
 171 formed in the fluoride electrolyte are characterized by different morphological parameters
 172 (diameter, thickness, length,...) that can be confirmed from Figure 1e and f.

173
174 **Figure 2.**

175
176 The EDS analysis also shows that Al and V values are lower compared to the TA6V alloy,
 177 which can be explained by the oxidation of these elements to form the thin oxide layers of
 178 Al₂O₃ and V₂O₅ (or VO₂) respectively (Gibran et al., 2018). Note that Al and V signals may
 179 come also from the bulk alloy, not only from the surface oxide layer (Benea et al., 2014). The
 180 presence of these layers improves the osseointegration and enhances the biocompatibility of
 181 the implant material (Jo et al., 2013). It can be noted that no trace of F can be detected
 182 suggesting that this element is not incorporated into the oxides during the anodization process.

183
184 **Table. 1.** Elemental composition of the pristine TA6V alloy and the anodized TA6V alloy
 185 obtained in fluoride ethylene glycol electrolyte carrying 20 wt% H₂O content.

187
188

189

190

191

192

193

194

Element	% Weight		% Atomic	
	Pristine	Anodized	Pristine	Anodized
	TA6V	TA6V	TA6V	TA6V
	Alloy	Alloy	Alloy	Alloy
Al	6.41	3.61	10.87	3.95
V	3.21	2.68	2.88	1.55
O	-	29.93	-	55.21
Ti	90.37	63.78	86.25	39.29

195

196 3.2. Structural properties

197 After anodization, the as-formed TiO₂ NTs at various water contents were annealed at 500 °C
198 for 3 hours to convert the amorphous compound into a crystalline structure. Figure 3 shows
199 the XRD patterns of these films. Compared to the as-anodized TiO₂ NTs using 20 wt% H₂O,
200 the crystallizations of the TiO₂ NTs films are mainly composed of anatase phase, as
201 evidenced by the diffraction peaks at $2\theta = 25.50, 37.80, 48.30$ and 55.10° . The diffraction
202 peaks can be indexed to the (101), (004), (200) and (211) planes, respectively (JCPDS Pattern
203 no 00-021-1272). Furthermore, the XRD patterns give no indication of the presence of the
204 Al₂O₃ and V₂O₅ (or VO₂) peaks due to their low percentage in the samples and the high
205 dispersion of metal ions in the nanotubular lattice (Li et al., 2009 ;Tang et al., 2014).

206

207

Figure 3.

208

209 3.3. Optical properties

210 Figure 4 (a-e) shows the optical absorption spectra of the annealed TiO₂ NTs at 500 °C for 3
211 hours obtained from anodization of TA6V alloy in fluoride EG electrolyte at different water
212 contents. The strong absorptions of these films in the range of 250 to 336 nm correspond to
213 the electron-transition from the valence band (VB) to the conduction band (CB) with creation
214 of two very reactive species, an electron in the CB and a hole in the VB (Hoffmann et al.,
215 1995). The UV absorption edge of samples prepared using 2, 5, 10, 15 and 20 wt% H₂O that
216 are around 332, 335, 340, 380, and 410 nm respectively, correspond to the maximum
217 absorption edge for each curves that are projected on the wavelength axis (nm). By increasing
218 the water content in the solution, the absorption band extends into the visible region. This
219 behavior explained by the increase of the active surface (number of reaction sites) with the
220 formation of TiO₂ NTs characterized by an improvement of their morphological parameters
221 (diameter, thickness, length ...) confirmed by the SEM images given in Figure 1e and f. In
222 addition, the presence of vanadium oxide in the structure is responsible for additional
223 impurity states in the band gap near the CB or the VB altering the optical properties of the
224 material (Chen et al., 2015; Li et al., 2009; Nešić et al., 2013). The same behavior was
225 obtained by the study of Luo et al. suggesting that the extends of absorption edge into the
226 visible region is attributed to the quantum size effects (Luo et al., 2008).

227 Evaluation of the TiO₂ NTs band gap (*E_g*) grown from anodization of Ti- 6Al- 4V alloy can
228 be obtained from the absorption coefficient α given in Equation (4) (Mane et al., 2005)

$$229 \quad \alpha = (h\nu - E_g)^{0.5} / h\nu \quad (4)$$

230 $\alpha = A / l$, where A is the absorption film, l is the tubes length ($l = 1.25 \mu\text{m}$) and $h\nu$ is the
231 photon energy. Figure 4f shows the variations of $(\alpha h\nu)^2$ versus photon energy ($h\nu$) for the film
232 synthesized using 20 wt% H₂O in the electrolyte. The extrapolation of the straight line to zero
233 absorption gives the effective band gap energy (*E_g*) value of approximately 2.25 eV, which is
234 significantly lower than that of TiO₂ anatase (~3.2 eV) (Li et al., 2013). The low band gap
235 value is explained by the presence of vanadium oxide that can extend the absorption band into
236 the visible region. This result is in agreement with the EDS analysis and the appearance of
237 yellow-green color in the annealed sample at 500 °C for 3 hours as shown in Figure 5b. The
238 color reflected on the annealed TiO₂ NTs sample at 20 wt% H₂O can be determined through
239 the UV absorption spectra. As seen, the lowest absorption spectra is approximately 500 nm,
240 reflecting a yellow-green color. In the agreement with the previous findings, the V-doped
241 TiO₂ materials were prepared by both sol-gel technique and liquid phase deposition (LPD)
242 reported that the presence of V can widen the absorption threshold wavelength to 650 nm
243 (Zhou et al., 2010 ; Gu et al., 2007).

244 **Figure 4.**

245 **Figure 5.**

249 3.4. Electrochemical Performance

250 In this work, self-organized TiO₂ NTs fabricated from TA6V alloy containing α and β phase
251 are investigated as a potential anode materials for Li-ion microbatteries. The electrochemical
252 performance of TiO₂ NTs synthesized using ethylene glycol electrolyte containing 20 wt%
253 H₂O is elucidated through cyclic voltammetry (CV) to analyse the charging and discharging
254 mechanisms during cycling. The anodic and cathodic peaks obtained during the
255 measurements represent the possible phase transformations or redox reactions with the
256 electrodes (Heinze, J., 1984). The TiO₂ NTs on TA6V alloy was tested at various scanning
257 rates (0.05, 0.1 and 0.5 mV.s⁻¹) between 1 and 3 V vs. Li/Li⁺ at room temperature, as
258 displayed in Figure 6 a. Two distinct cathodic and anodic peaks are observed for all scan
259 rates, corresponding to the lithium insertion (Ti⁴⁺ → Ti³⁺) and extraction (Ti³⁺ → Ti⁴⁺) in
260 anatase (Liu et al., 2012). At a scan rate of 0.05 mV.s⁻¹, the cathodic peak centered at ~1.74 V
261 vs. Li/Li⁺ and the anodic peak centered at 1.96 V vs. Li/Li⁺ show a peak potential separation (ΔE_p)
262 of 0.22 V. The cathodic and anodic peak slightly shifted to 1.73 V vs. Li/Li⁺ and 1.97 V
263 vs. Li/Li⁺, respectively at 0.1 mV.s⁻¹, showing the ΔE_p of 0.24 V. Further higher scan rate of
264 0.5 mV.s⁻¹, the cathodic and anodic peaks are significantly shifted to ~1.71 V vs. Li/Li⁺ and
265 ~2.03 V vs. Li/Li⁺, respectively with the ΔE_p of 0.32 V. Obviously, as the scan rate was
266 increased, the displacement current increased due to the fact that the over potential become
267 higher.

268 **Figure 6.**

271 The separation between the cathodic and anodic peaks indicated the extent of polarization.
272 Hence, the slow scan rate is selected to establish an electrochemical equilibrium between the
273 active species due to the fast scan rate might provoke peak identification more difficult

274 (Pylahan et al., 2015). In addition to the main peaks, an additional peak pair at a potential of
 275 ~ 2.55 V vs. Li/Li⁺ with a low current density is showed up in the reduction and oxidation
 276 potential at three different scan rates. It is due to the presence of an electrochemically active
 277 vanadium oxide with low valence state of vanadium such as VO₂ phase (Mattelaer et al.,
 278 2017; Mai et al., 2010). The formation of nanotubes on two phases ($\alpha + \beta$) titanium alloys
 279 leads to the selective dissolution of the elements and the different reactions rates at different
 280 phases, yielding VO₂ and Al₂O₃ phases. Considering the peak intensity of VO₂ with respect to
 281 anatase TiO₂ NTs, it is assumed that the VO₂ phase might not contribute significantly to the
 282 storage performance of the electrode. Apart from both peak pairs, no additional peak for the
 283 Al₂O₃ phase can be detected in the CVs curves as this phase is probably to be
 284 electrochemically inactive. Furthermore, cyclic voltammograms at low scan rate of both 0.05
 285 and 0.1 mV.s⁻¹ for 10 cycles reveal a good stability of the electrode which is attested by no
 286 peak shifting (see Figure 6b-c). The main cathodic and anodic peaks can be clearly identified
 287 up to the 10th cycle.

288
 289 The charge-discharge behaviors of the alloyed TiO₂ NTs were examined by galvanostatic tests
 290 between cut-off voltages of 1 and 3 V vs Li/Li⁺. The results are shown in Figure 7a. It is
 291 found that in the first discharge process, there is a short plateau at ~ 2.55 V which indicates a
 292 very small amount of Li ions inserted into VO₂ phase with a low storage capacity. This
 293 plateau is in good accordance with the cyclic voltammogram curve. The potential
 294 continuously drops and reaches the large constant plateau at ~ 1.77 V which is attributed to
 295 homogeneous Li insertion into the bulk anatase with a lithium insertion capacity of about 85
 296 mAh.g⁻¹ (36 μ Ah.cm⁻². μ m⁻¹). The slope after the plateau, started from ~ 1.77 V to 1 V has the
 297 insertion capacity of 183 mAh.g⁻¹ (77 μ Ah.cm⁻². μ m⁻¹), which is attributed to the energy
 298 capacity accumulated on the surface of anatase. The lithium extraction capacity is solely
 299 about 20 mAh.g⁻¹ within the charging potential window of 1–1.84 V in the first cycle, which
 300 is smaller than the capacity in the discharging potential region of 1.77–1 V. This results
 301 indicates that the irreversible capacity mainly occurs within the sloped region between 1.77
 302 and 1V. However, the main voltage plateaus consist of the discharge plateau at ~ 1.77 V vs.
 303 Li/Li⁺ and a charge plateau at ~ 1.84 V vs. Li/Li⁺, resulting in a very small polarization of 0.07
 304 V at C/10 rate. In a good agreement with previous results, the charge plateau at ~ 1.89 V vs.
 305 Li/Li⁺ and discharge plateau at ~ 1.75 V vs. Li/Li⁺ with a higher polarization of 0.14 V at C/10
 306 rate are obtained for the self-organized TiO₂ NTs synthesized in a solution of ethylene glycol
 307 containing 1.0 wt% H₂O and 2 wt% NH₄F (Prosini et al., 2013). The smaller difference of the
 308 charge and discharge plateaus indicates the better electrode reaction kinetics and better rate
 309 performance. The reversible Li⁺ insertion into TiO₂ NTs can be written according to Equation
 310 (5) (Djenizian et al., 2011).



312
 313 Taking the middle points between these two plateaus, the average working potentials of cell
 314 were determined to be ~ 1.80 V vs. Li/Li⁺. The high working potential of the nanotubes is an
 315 advantage to avoid the electrolyte reduction and limit the formation of a solid electrolyte
 316 interphase (SEI) layer on the surface of the electrode (Xu et al., 2007).

317
 318 The electrochemical reaction at the anode is based on the reduction of Ti⁴⁺ to Ti³⁺ and the Li⁺
 319 insertion into the TiO₂ NTs. Lithium ions can be inserted reversibly into anatase TiO₂ to form
 320 Li_{0.5}TiO₂, giving a theoretical specific capacity of 168 mAh.g⁻¹ while the theoretical capacity
 321 of amorphous TiO₂ NTs is 335 mAh.g⁻¹ for the insertion of one Li per Ti unit (Auer et al.,
 322 2018). In this study, the obtained initial discharge and charge capacities of the electrodes are
 323

324 288 mAh.g⁻¹ (122 μAh.cm⁻².μm⁻¹) and 142 mAh.g⁻¹ (60 μAh.cm⁻².μm⁻¹), corresponding to the
325 lithium insertion coefficient of 0.86 and 0.42, respectively with a relatively low initial
326 coulombic efficiency of 49.30 %. A high capacity of anatase TiO₂ NTs in the first few initial
327 cycles is probably due to the presence of the remaining amorphous nanotubes (Prosini et al.,
328 2013).

329

330

331

Figure 7.

332 For the subsequent cycles, the discharge capacity values recorded in the 2nd and 10th cycles
333 are 186 mAh.g⁻¹ and 150 mAh.g⁻¹ with an improved coulombic efficiency of 76.34 % and
334 94.67 %, respectively. The capacity fading from the 2nd to the 10th cycle can be attributed to
335 an irreversible reaction of Li⁺ ions with OH groups existing on the surface of nanotubes at
336 low voltages (Ferrari et al., 2017). In addition, the initial capacity loss may also be caused by
337 the interfacial reaction between the residual traces of water on the surface of the nanotubes
338 and lithium salt in the electrolyte combined with the presence of structural defects (Chung et
339 al., 2015; Hanzu et al., 2011). However, the cycling retention continuously improved after
340 first few cycles, thereby coulombic efficiency approaches 100%.

341

342 The cells were cycled at multiple C-rates as presented in Figure 7b. TiO₂ NTs electrode gives
343 a stable capacity of 150 mAh.g⁻¹ (63 μAh.cm⁻².μm⁻¹) at C/10, 134 mAh.g⁻¹ (56 μAh.cm⁻².μm⁻¹)
344 at C/5, 101 mAh.g⁻¹ (43 μAh.cm⁻².μm⁻¹) at C/2 and 83 mAh.g⁻¹ (35 μAh.cm⁻².μm⁻¹) at 1C.
345 The capacity can be recovered after cycling at C/10 rate over 50 cycles. We noted that the
346 capacity loss at C/10 rate after cycling at fast kinetic rates is attributed to the hindered
347 migration of Li⁺ ions within the TiO₂ NTs system due to the presence of other crystalline
348 phases. However, it can be observed that the capacity of two last cycles are enough stable at
349 C/10 rate, hence we assumed the discharge capacities stabilize after few initial cycles. To
350 prove the cycling stability of the TiO₂ NTs, galvanostatic charge-discharge were performed at
351 1C rate up to 50 cycles (Figure 7c and d). The results thus clearly show a good cycling
352 stability of the TiO₂ NTs electrodes that can deliver a reversible capacity of 82 mAh.g⁻¹ (34
353 μAh.cm⁻².μm⁻¹).

354

355

356 4. Conclusion

357 In summary, self-organized TiO₂ NTs have been successfully synthesized via anodization of
358 Ti-6Al-4V alloy at 60 V for 3 hours in fluoride ethylene glycol electrolyte at various water
359 contents (2 wt% up to 20wt% H₂O). Significant differences in morphological structure of
360 TiO₂ NTs were obtained. At low water content, a honeycomb and porous structure is formed
361 on the surface due to the presence of both α and β phases in the Ti-6Al-4V alloy leading to a
362 dissimilar non-uniform etching. Remarkably, self-organized TiO₂ NTs could be formed
363 uniformly across both α and β phases at 20 wt% H₂O. The optical properties and
364 electrochemical performance of the anodized TiO₂ NTs carrying 20 wt% H₂O have been
365 investigated. The anatase TiO₂ NTs offers a low band gap value equal to 2.25 eV due to the
366 presence of vanadium oxide in the structure that widens the threshold of absorption
367 wavelength into the visible region. Moreover, galvanostatic charge-discharge tests exhibited a
368 good capacity of 82 mAh.g⁻¹ (34 μAh.cm⁻².μm⁻¹) at 1C rate over 50 cycles. These results
369 show that the self organized TiO₂ NTs grown from TA6V alloy can be considered as
370 competitive anode materials for Li-ion microbatteries, as well as other potential applications
371 in gas sensors, solar cells, and photocatalysis.

372

373

374 **Author Contribution**

375 HF and VA S performed experiments, analyzed the experimental results and wrote the
376 manuscript. DH, M SB, FV, ME, MP and TD discussed experimental results. All the authors
377 contributed to the reading of paper and gave advice on the revision of the manuscript.

378

379 **Conflict of Interest Statement**

380 The authors declare that the research was conducted in the absence of any commercial or
381 financial relationships that could be construed as a potential conflict of interest.

382

383 **Acknowledgment**

384 This work is carried out with the contribution of the cooperation project N ° 16 MDU 970;
385 Mixed Evaluation and Prospective Commission - Hubert Curien Program (CMEP-PHC)
386 TASSILI.

387

388

389 **References**

- 390 Armstrong, A. R., Armstrong, G., Canales, J., García, R., and Bruce, P. G. (2005). Lithium-
391 Ion Intercalation into TiO₂-B Nanowires. *Adv. Mater.* 17, 862–865.
392 doi:10.1002/adma.200400795
- 393 Auer, A., Steiner, D., Portenkirchner, E., and Kunze-Liebhäuser, J. (2018). Nonequilibrium
394 Phase Transitions in Amorphous and Anatase TiO₂ Nanotubes. *ACS Appl. Energy Mater.*
395 1, 1924–1929. doi:10.1021/acsaem.7b00319
- 396 Benea, L., Mardare-Danaila, E., Mardare, M., and Celis, J.-P. (2014). Preparation of titanium
397 oxide and hydroxyapatite on Ti–6Al–4V alloy surface and electrochemical behaviour in
398 bio-simulated fluid solution. *Corrosion Science* 80, 331–338.
399 doi:10.1016/j.corsci.2013.11.059.
- 400 Black, J., and Hastings, G. (2013). *Handbook of Biomaterial Properties*, Springer Science &
401 Business Media.
- 402 Chang, Y. C., Peng, C. W., Chen, P. C., Lee, C. Y., and Chiu, H. T. (2015). Bio-ingredient
403 assisted formation of porous TiO₂ for Li-ion battery electrodes. *RSC Adv.* 5, 34949-
404 34955. doi.org/10.1039/C5RA04896F
- 405 Chen, Y. W., Chang, J. Y., and Moongraksathum, B. (2015). Preparation of vanadium-doped
406 titanium dioxide neutral sol and its photocatalytic applications under UV light
407 irradiation. *J. Taiwan Inst. Chem. Eng.* 52, 140-146. doi:10.1016/j.jtice.2015.02.006.
- 408 Choi, J., Park, H., and Hoffmann, M. R. (2009). Effects of Single Metal-Ion Doping on the
409 Visible-Light Photoreactivity of TiO₂. *J. Phys. Chem. C*, 114, 783–792.
410 doi:10.1021/jp908088x
- 411 Chung, D. Y., Chung, Y.-H., Kim, S., Lim, J. W., Lee, K. J., Jung, N., et al. (2015).
412 Understanding Interface between Electrode and Electrolyte: Organic/Inorganic Hybrid
413 Design for Fast Ion Conductivity. *J Phys Chem C*, 119, 9169–9176.
414 doi:10.1021/acs.jpcc.5b02075

415 Das, S. K., Gnanavel, M., Patel, M. U. M., Shivakumara, C., and Bhattacharyya, A. J. (2011).
416 Anomolously High Lithium Storage in Mesoporous Nanoparticulate Aggregation of Fe³⁺
417 Doped Anatase Titania. *J. Electrochem. Soc.* 158, A1290. doi:10.1149/2.029112jes
418 Djenizian, T., Hanzu, I., and Knauth, P. (2011). Nanostructured negative electrodes based on
419 titania for Li-ion microbatteries. *J. Mater. Chem.* 21, 9925-9937.
420 doi:10.1039/C0JM04205F
421 Duan, J., Hou, H., Liu, X., Yan, C., Liu, S., Meng, R., et al. (2016). In situ Ti³⁺-doped TiO₂
422 nanotubes anode for lithium ion battery. *J. Porous Mater.* 23, 837-843.
423 doi:10.1007/s10934-016-0139-6
424 Ellis, B. L., Knauth, P., and Djenizian, T. (2014). Three-Dimensional Self-Supported Metal
425 Oxides for Advanced Energy Storage. *Adv. Mater.* 26, 3368-3397.
426 doi:10.1002/adma.201306126
427 Fang, H. T., Liu, M., Wang, D. W., Sun, T., Guan, D. S., Li, F., et al. (2009). Comparison of
428 the rate capability of nanostructured amorphous and anatase TiO₂ for lithium insertion
429 using anodic TiO₂ nanotube arrays. *Nanotechnology*, 20, 225701. doi.org/10.1088/0957-
430 4484/20/22/225701
431 Ferrari, I. V., Braglia, M., Djenizian, T., Knauth, P., and Di Vona, M. L. (2017).
432 Electrochemically engineered single Li-ion conducting solid polymer electrolyte on
433 titania nanotubes for microbatteries. *J. Power Sources* 353, 95-103.
434 doi.org/10.1016/j.jpowsour.2017.03.141
435 Gibran, K., Ibadurrahman, M., and Slamet. (2018). Effect of electrolyte type on the
436 morphology and crystallinity of TiO₂ nanotubes from Ti-6Al-4V anodization. *IOP Conf.*
437 *Ser. Earth Environ. Sci.* 105, 012038. doi:10.1088/1755-1315/105/1/012038
438 Gu, D.-E., Yang, B.-C., and Hu, Y.-D. (2007). A Novel Method for Preparing V-doped
439 Titanium Dioxide Thin Film Photocatalysts with High Photocatalytic Activity Under
440 Visible Light Irradiation. *Catal. Lett.* 118, 254-259. doi:10.1007/s10562-007-9179-5
441 Hanzu, I., Djenizian, T., and Knauth, P. (2011). Electrical and Point Defect Properties of TiO₂
442 Nanotubes Fabricated by Electrochemical Anodization. *J Phys Chem C*, 115, 5989-5996.
443 doi:10.1021/jp1111982
444 Heinze, J. (1984). Cyclic Voltammetry—"Electrochemical Spectroscopy". New Analytical
445 Methods(25). *Angew. Chem., Int. Ed. Engl.* 23, 831-847. doi:10.1002/anie.198408313
446 Hoffmann, M. R., Martin, S. T., Choi, W., and Bahnemann, D. W. (1995). Environmental
447 applications of semiconductor photocatalysis. *Chem. Rev.* 95, 69-
448 96. doi:10.1021/cr00033a004
449 Jo, C.-I., Jeong, Y.-H., Choe, H.-C., and Brantley, W. A. (2013). Hydroxyapatite precipitation
450 on nanotubular films formed on Ti-6Al-4V alloy for biomedical applications. *Thin Solid*
451 *Films*, 549, 135-140. doi:10.1016/j.tsf.2013.09.095
452 Kyeremateng, N. A., Vacandio, F., Sougrati, M. T., Martinez, H., Jumas, J. C., Knauth, P., et
453 al. (2013b). Effect of Sn-doping on the electrochemical behaviour of TiO₂ nanotubes as
454 potential negative electrode materials for 3D Li-ion micro batteries. *J. Power.*
455 *Sources.* 224, 269-277. doi:10.1016/j.jpowsour.2012.09.104
456 Kyeremateng, N. A., Plylahan, N., dos Santos, A. C., Taveira, L. V., Dick, L. F., and
457 Djenizian, T. (2013a). Sulfidated TiO₂ nanotubes: A potential 3D cathode material for Li-
458 ion micro batteries. *Chem. Commun.* 49, 4205-4207. doi:10.1039/c2cc36857a
459 Li, H., Martha, S. K., Unocic, R. R., Luo, H., Dai, S., and Qu, J. (2012). High cyclability of
460 ionic liquid-produced TiO₂ nanotube arrays as an anode material for lithium-ion
461 batteries. *J. Power Source* s218, 88-92. doi.org/10.1016/j ;jpowsour.2012.06.096
462 Li, J., Du, Z., Ruther, R. E., An, S. J., David, L. A., Hays, K., et al. (2017). Toward low-cost,
463 high-energy density, and high-power density lithium-ion batteries. *JOM-US*69, 1484-
464 1496. doi:10.1007/s11837-017-2404-9

465 Li, L., Liu, C. Y., and Liu, Y. (2009). Study on activities of vanadium (IV/V) doped TiO₂ (R)
466 nanorods induced by UV and visible light. *Mater. Chem. Phys.* 113, 551-557.
467 doi.org/10.1016/j.matchemphys.2008.08.009.

468 Lin, S.-H., Ou, C.-C., Su, M.-D., and Yang, C.-S. (2013). Photo-catalytic behavior of vanadia
469 incorporated titania nanoparticles. *Catal. Sci. Technol.* 3, 2081–2091.
470 doi:10.1039/c3cy00053b

471 Li, Z., Ding, D., Liu, Q., and Ning, C. (2013). Hydrogen Sensing with Ni-Doped TiO₂
472 Nanotubes. *Sensors (Basel)* 13, 8393–8402. doi:10.3390/s130708393.

473 Long, M., and Rack, H. J. (1998). Titanium alloys in total joint replacement—a materials
474 science perspective. *Biomaterials*, 19, 1621–1639. doi:10.1016/s0142-9612(97)00146-4

475 Luo, B., Yang, H., Liu, S., Fu, W., Sun, P., Yuan, M., et al. (2008). Fabrication and
476 characterization of self-organized mixed oxide nanotube arrays by electrochemical
477 anodization of Ti-6Al-4V alloy. *Mater. Lett.* 62, 4512–4515.
478 doi:10.1016/j.matlet.2008.08.015

479 Macak, J. M., Tsuchiya, H., Taveira, L., Ghicov, A., and Schmuki, P. (2005). Self-organized
480 nanotubular oxide layers on Ti-6Al-7Nb and Ti-6Al-4V formed by anodization in NH₄F
481 solutions. *J. Biomed. Mater. Res., Part A* 75, 928–933. doi:10.1002/jbm.a.30501

482 Mai, L., Xu, L., Han, C., Xu, X., Luo, Y., Zhao, S., et al. (2010). Electrospun Ultralong
483 Hierarchical Vanadium Oxide Nanowires with High Performance for Lithium Ion
484 Batteries. *Nano Lett.* 10, 4750–4755. doi:10.1021/nl103343w

485 Mane, R. S., Lee, W. J., Pathan, H. M., and Han, S. H. (2005). Nanocrystalline TiO₂/ZnO thin
486 films: fabrication and application to dye-sensitized solar cells. *J. Phys. Chem. B* 109,
487 24254-24259. DOI: 10.1021/jp0531560.

488 Mattelaer, F., Geryl, K., Rampelberg, G., Dendooven, J., and Detavernier, C. (2017).
489 Amorphous and Crystalline Vanadium Oxides as High-Energy and High-Power Cathodes
490 for Three-Dimensional Thin-Film Lithium Ion Batteries. *ACS Appl. Mater. Interfaces*, 9,
491 13121–13131. doi:10.1021/acsami.6b16473

492 Matykina, E., Hernandez-López, J. M., Conde, A., Domingo, C., de Damborenea, J. J., and
493 Arenas, M. A. (2011). Morphologies of nanostructured TiO₂ doped with F on Ti-6Al-4V
494 alloy. *Electrochim. Acta*, 56, 2221–2229. doi:10.1016/j.electacta.2010.11.069

495 Moravec, H., Vandrovcova, M., Chotova, K., Fojt, J., Pruchova, E., Joska, L., et al. (2016).
496 Cell interaction with modified nanotubes formed on titanium alloy Ti-6Al-4V. *Mater. Sci.*
497 *Eng. C* 65, 313–322. doi:10.1016/j.msec.2016.04.037

498 Morozová, M., Kluson, P., Krysa, J., Vesely, M., Dzik, P., and Solcova, O. (2012).
499 Electrochemical properties of TiO₂ electrode prepared by various methods. *Procedia.*
500 *Eng.* 42, 573-580. doi.org/10.1016/j.proeng.2012.07.450.

501 Nešić, J., Manojlović, D. D., Anđelković, I., Dojčinović, B. P., Vulić, P. J., Krstić, J., et
502 Roglić, G. M. (2013). Preparation, characterization and photocatalytic activity of
503 lanthanum and vanadium co-doped mesoporous TiO₂ for azo-dye degradation. *J. Mol.*
504 *Catal. A: Chem.* 378, 67-75. doi:10.1016/j.molcata.2013.05.018.

505 Ortiz, G. F., Hanzu, I., Djenizian, T., Lavela, P., Tirado, J. L., and Knauth, P. (2008).
506 Alternative Li-ion battery electrode based on self-organized titania nanotubes. *Chem.*
507 *Mater.* 21, 63-67. doi:10.1021/cm801670u

508 Ortiz, G. F., Hanzu, I., Knauth, P., Lavela, P., Tirado, J. L., and Djenizian, T. (2009). TiO₂
509 nanotubes manufactured by anodization of Ti thin films for on-chip Li-ion 2D
510 microbatteries. *Electrochim. Acta* 54, 4262-4268. doi:10.1016/j.electacta.2009.02.085

511 Panda, S. K., Yoon, Y., Jung, H. S., Yoon, W. S., and Shin, H. (2012). Nanoscale size effect
512 of titania (anatase) nanotubes with uniform wall thickness as high performance anode for
513 lithium-ion secondary battery. *J. Power. Sources.* 204, 162
514 167. doi:10.1016/j.jpowsour.2011.12.048

515 Pansila, P., Witit-Anun, N., and Chaiyakun, S. (2012). Influence of sputtering power on
516 structure and photocatalyst properties of DC magnetron sputtered TiO₂ thin
517 film. *Procedia. Eng.* 32, 862-867. doi.org/10.1016/j.proeng.2012.02.024

518 Pikul, J. H., Zhang, H. G., Cho, J., Braun, P. V., and King, W. P. (2013). High-power lithium
519 ion microbatteries from interdigitated three-dimensional bicontinuous nanoporous
520 electrodes. *Nat. Commun.* 4, 1732. doi:10.1038/ncomms2747

521 Plylahan, N., Kyeremateng, N. A., Eyraud, M., Dumur, F., Martinez, H., Santinacci, L., et al.
522 (2012). Highly conformal electrodeposition of copolymer electrolytes into titania
523 nanotubes for 3D Li-ion batteries. *Nanoscale Res. Lett.* 7, 349. doi:10.1186/1556-276x-7-
524 349

525 Plylahan, N., Letiche, M., Barr, M. K. S., and Djenizian, T. (2014). All-solid-state lithium-ion
526 batteries based on self-supported titania nanotubes. *Electrochem. Commun.* 43, 121-124.
527 doi:10.1016/j.elecom.2014.03.029

528 Plylahan, N., Demoulin, A., Chrystelle Lebouin, C. L., Knauth, P., and Djenizian, T. (2015).
529 Mechanism study of Li⁺ insertion into titania nanotubes. *RSC Adv.* 5, 28474–28477.
530 doi:10.1039/c5ra03759j

531 Prosini, P. P., Cento, C., and Pozio, A. (2013). Lithium-ion batteries based on titanium oxide
532 nanotubes and LiFePO₄. *J. Solid State Electrochem.* 18, 795–804. doi:10.1007/s10008-
533 013-2324-8

534 Reszczyńska, J., Grzyb, T., Sobczak, J. W., Lisowski, W., Gazda, M., Ohtani, B., et al.
535 (2014). Lanthanide co-doped TiO₂: the effect of metal type and amount on surface
536 properties and photocatalytic activity. *Appl. Surf. Sci.* 307, 333-345.
537 doi.org/10.1016/j.apsusc.2014.03.199

538 Salian, G. D., Koo, B. M., Lefevre, C., Cottineau, T., Lebouin, C., Tesfaye, A. T., et al.
539 (2018). Niobium Alloying of Self-Organized TiO₂ Nanotubes as an Anode for Lithium-
540 Ion Microbatteries. *Adv. Mater. Technol.* 3, 1700274. doi:10.1002/admt.201700274

541 Salian, G. D., Lebouin, C., Demoulin, A., Lepihin, M. S., Maria, S., Galeyeva, A. K., et al.
542 (2017). Electrodeposition of polymer electrolyte in nanostructured electrodes for
543 enhanced electrochemical performance of thin-film Li-ion microbatteries. *J. Power*
544 *Sources*, 340, 242-246. doi:10.1016/j.jpowsour.2016.11.078

545 Sopha, H., Salian, G. D., Zazpe, R., Prikryl, J., Hromadko, L., Djenizian, T., et al. (2017).
546 ALD Al₂O₃-Coated TiO₂ Nanotube Layers as Anodes for Lithium-Ion Batteries. *ACS*
547 *Omega*, 2, 2749–2756. doi:10.1021/acsomega.7b00463

548 Sugiawati, V. A., Vacandio, F., Eyraud, M., Knauth, P., and Djenizian, T. (2016). Porous
549 NASICON-Type Li₃Fe₂(PO₄)₃ Thin Film Deposited by RF Sputtering as Cathode
550 Material for Li-Ion Microbatteries. *Nanoscale Res. Lett.* 11. doi:10.1186/s11671-016-
551 1574-7

552 Sugiawati, V. A., Vacandio, F., Knauth, P., and Djenizian, T. (2018). Sputter-Deposited
553 Amorphous LiCuPO₄ Thin Film as Cathode Material for Li-ion Microbatteries.
554 *ChemistrySelect* 3, 405-409. doi:10.1002/slct.201702429

555 Tang, D., Wang, Y., Zhao, Y., Yang, Y., Zhang, L., and Mao, X. (2014). Effect of the
556 composition of Ti alloy on the photocatalytic activities of Ti-based oxide nanotube arrays
557 prepared by anodic oxidation. *Appl. Surf. Sci.* 319, 181–188.
558 doi:10.1016/j.apsusc.2014.07.149

559 Xiong, W., Xia, Q., and Xia, H. (2014). Three-dimensional self-supported metal oxides as
560 cathodes for microbatteries. *Funct. Mater. Lett.* 7, 1430003.
561 doi:10.1142/S1793604714300035

562 Xu, J., Jia, C., Cao, B., and Zhang, W. F. (2007). Electrochemical properties of anatase TiO₂
563 nanotubes as an anode material for lithium-ion batteries. *Electrochim. Acta*, 52, 8044–
564 8047. doi:10.1016/j.electacta.2007.06.077

565 Yu, C., Bai, Y., Yan, D., Li, X., and Zhang, W. (2014). Improved electrochemical properties
566 of Sn-doped TiO₂ nanotube as an anode material for lithium ion battery. *J. Solid State*
567 *chem.* 18, 1933–1940. doi:10.1007/s10008-014-2436-9
568 Zhou, W., Liu, Q., Zhu, Z., and Zhang, J. (2010). Preparation and properties of vanadium-
569 doped TiO₂ photocatalysts. *J. Phys. D: Appl. Phys.* 43, 035301. doi:10.1088/0022-
570 3727/43/3/035301
571

572 **Figure 1.** SEM images of TiO₂ NTs obtained from anodization of TA6V alloy in fluoride
573 ethylene glycol electrolyte with different water contents: 2 wt% (a), 5 wt% (b), 10 wt% (c),
574 15 wt% (d) and 20 wt% (e). Tilted view of TiO₂ NTs synthesized in 20 wt% H₂O (f).

575
576 **Figure 2.** EDS spectra of: pristine TA6V alloy (a) and anodized TA6V alloy in fluoride
577 ethylene glycol electrolyte with 20wt% H₂O content (b).
578

579 **Figure 3.** XRD patterns of TiO₂ NTs grown on TA6V alloy: as-anodized (a), films annealed
580 at 500 °C for 3 hours with the water content in the electrolyte is: 2 wt% H₂O (b), 10 wt%
581 H₂O (c), 5 wt% H₂O (d), 15 wt% H₂O (e) and 20 wt% H₂O (f). “A” is Anatase, “Ti” is
582 substrate of film.

583 **Figure 4.** UV-Vis absorption spectra of annealed TiO₂ NTs layers grown from anodization of
584 TA6V alloys at 60V for 3 hours in fluoride ethylene glycol electrolyte with different water
585 contents: 2wt%H₂O (a), 5wt%H₂O (b), 10wt%H₂O (c), 15wt%H₂O (d) and 20wt%H₂O (e).
586 Variations of $(\alpha h\nu)^2$ versus photon energy $(h\nu)$ of TiO₂ NTs synthesized with 20wt% H₂O in
587 the fluoride ethylene glycol electrolyte (f).

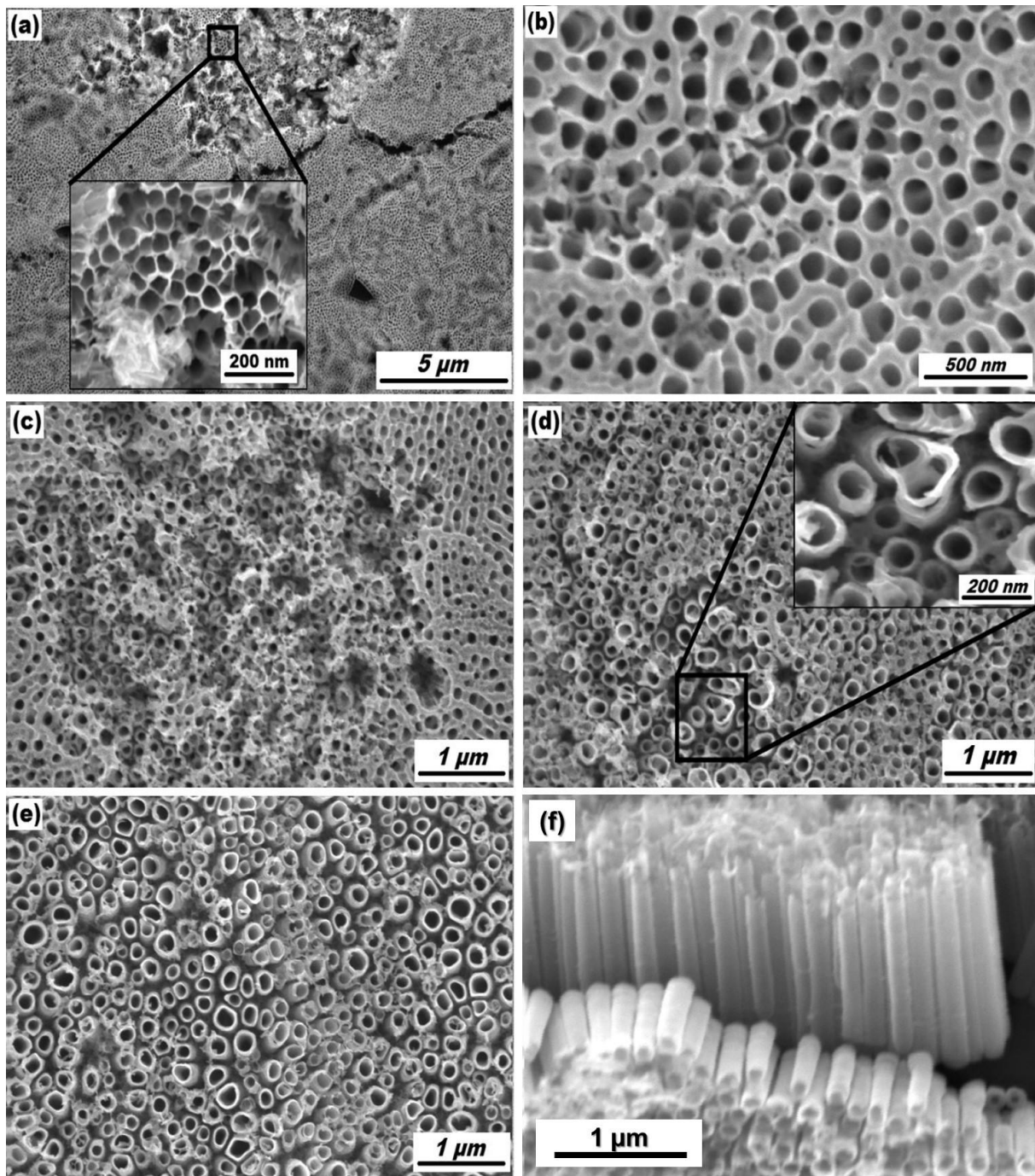
588
589 **Figure 5.** Ti-6Al-4V alloys anodized in fluoride ethylene glycol electrolyte with 20 wt%H₂O
590 at 60V for 3 hours: as-formed (a) and annealed at 500 °C for 3 hours (b).

591
592 **Figure 6.** Cyclic voltammograms of anatase TiO₂ NTs on Ti-6Al-4V alloy performed in the
593 potential range 1-3 V at a scan rate of 0.05 mV.s⁻¹, 0.1 mV.s⁻¹ and 0.5 mV.s⁻¹ (a), 10 cycles
594 CVs at scan rate of 0.05 mV.s⁻¹(b) and 10 cycles CVs at scan rate of 0.1 mV.s⁻¹(c).

595
596 **Figure 7.** Charge-discharge profile of anatase TiO₂ NTs on Ti-6Al-4V alloy at C/10 rate (a)
597 and the discharge capacity vs. cycle number at multiple C-rates (b), Charge-discharge profile
598 of anatase TiO₂ NTs on Ti-6Al-4V alloy at 1C rate (c) and cycling performance of anatase
599 TiO₂ NTs on Ti-6Al-4V alloy at 1C rate (d)

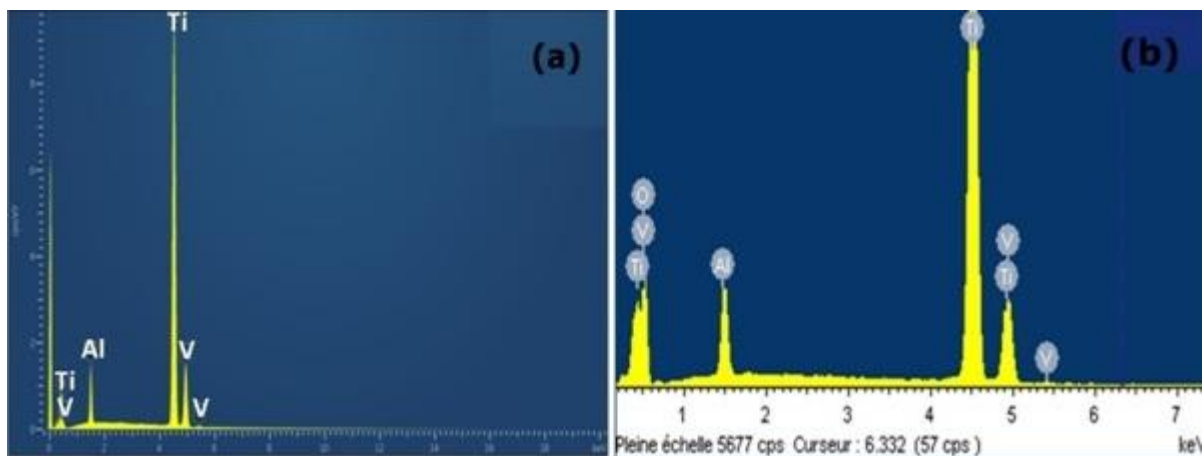
600

601

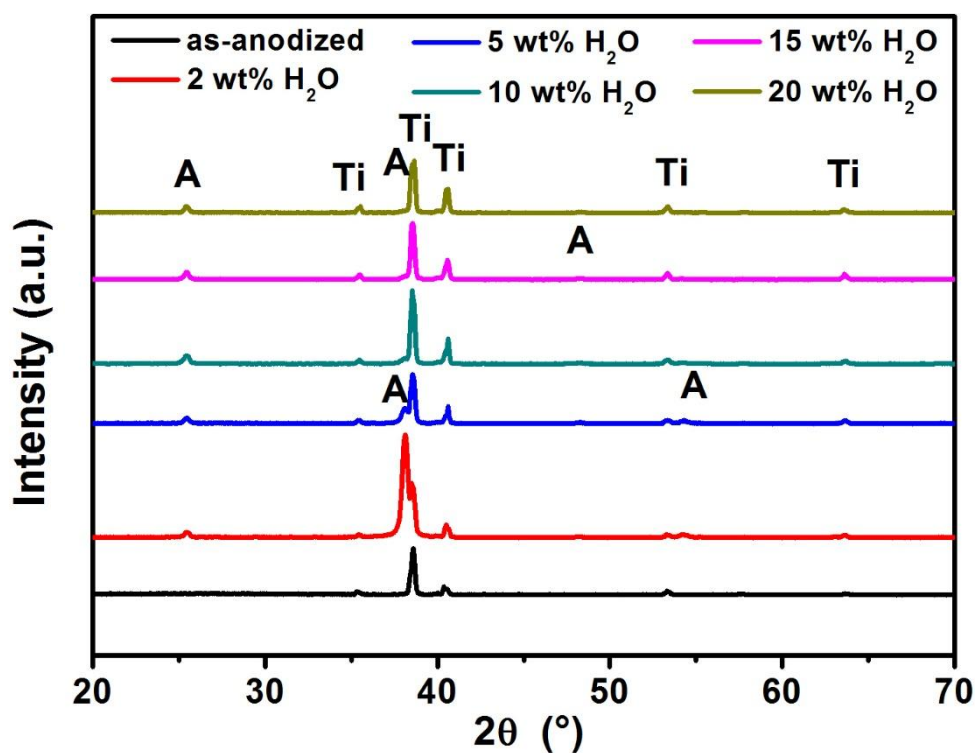


602

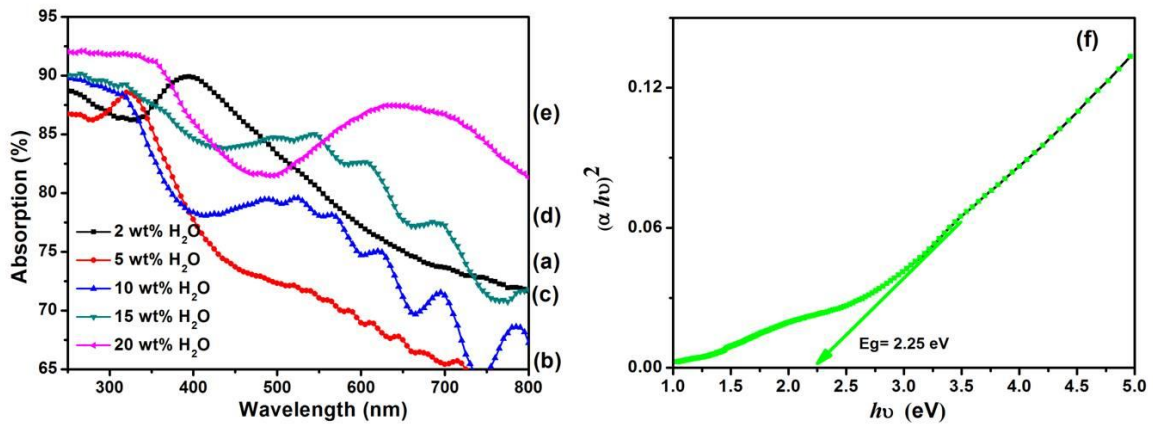
603 **Figure 1.** SEM images of TiO₂ NTs obtained from anodization of TA6V alloy in fluoride
 604 ethylene glycol electrolyte with different water contents: 2 wt% (a), 5 wt% (b), 10 wt% (c),
 605 15 wt% (d) and 20 wt% (e). Tilted view of TiO₂ NTs synthesized in 20 wt% H₂O (f).



606
 607 **Figure 2.** EDS spectra of: pristine TA6V alloy (a) and anodized TA6V alloy in fluoride
 608 ethylene glycol electrolyte with 20wt% H₂O content (b).



609
 610 **Figure 3.** XRD patterns of TiO₂ NTs grown on TA6V alloy: as-anodized (a), films annealed
 611 at 500 °C for 3 hours with the water content in the electrolyte is: 2 wt% H₂O (b), 10 wt%
 612 H₂O (c), 5 wt% H₂O (d), 15 wt% H₂O (e) and 20 wt% H₂O (f). “A” is Anatase, “Ti” is
 613 substrate of film.

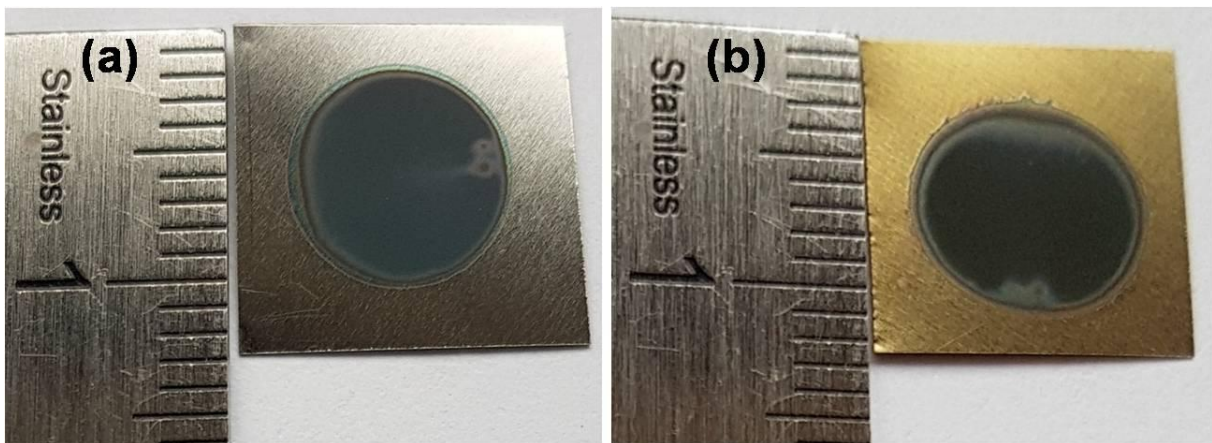


614

615 **Figure 4.** UV-Vis absorption spectra of annealed TiO₂ NTs layers grown from anodization of
 616 TA6V alloys at 60V for 3h in fluoride ethylene glycol electrolyte with different water
 617 contents: 2wt%H₂O (a), 5wt%H₂O (b), 10wt%H₂O (c), 15wt%H₂O (d) and 20wt%H₂O (e).
 618 Variations of $(\alpha h\nu)^2$ versus photon energy ($h\nu$) of TiO₂ NTs synthesized with 20wt% H₂O in
 619 the fluoride ethylene glycol electrolyte (f).

620

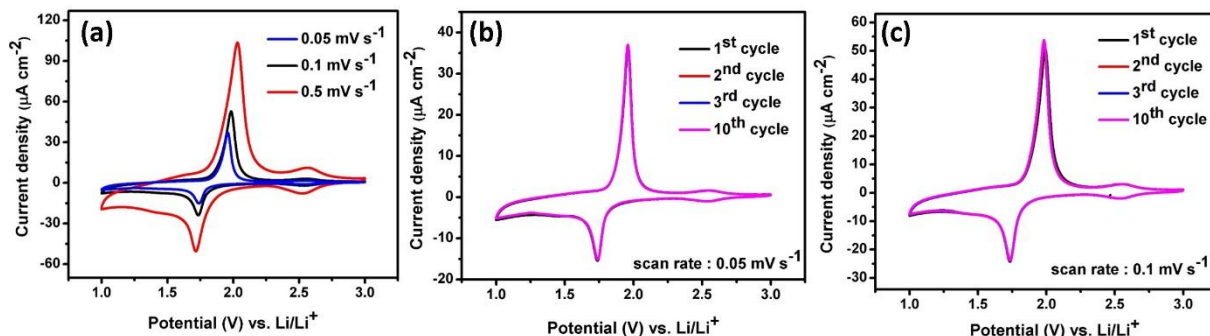
621



622

623 **Figure 5.** Ti-6Al-4V alloys anodized in fluoride ethylene glycol electrolyte with 20 wt%H₂O
 624 at 60V for 3 hours: as-formed (a) and annealed at 500 °C for 3 hours (b).
 625
 626

627



628

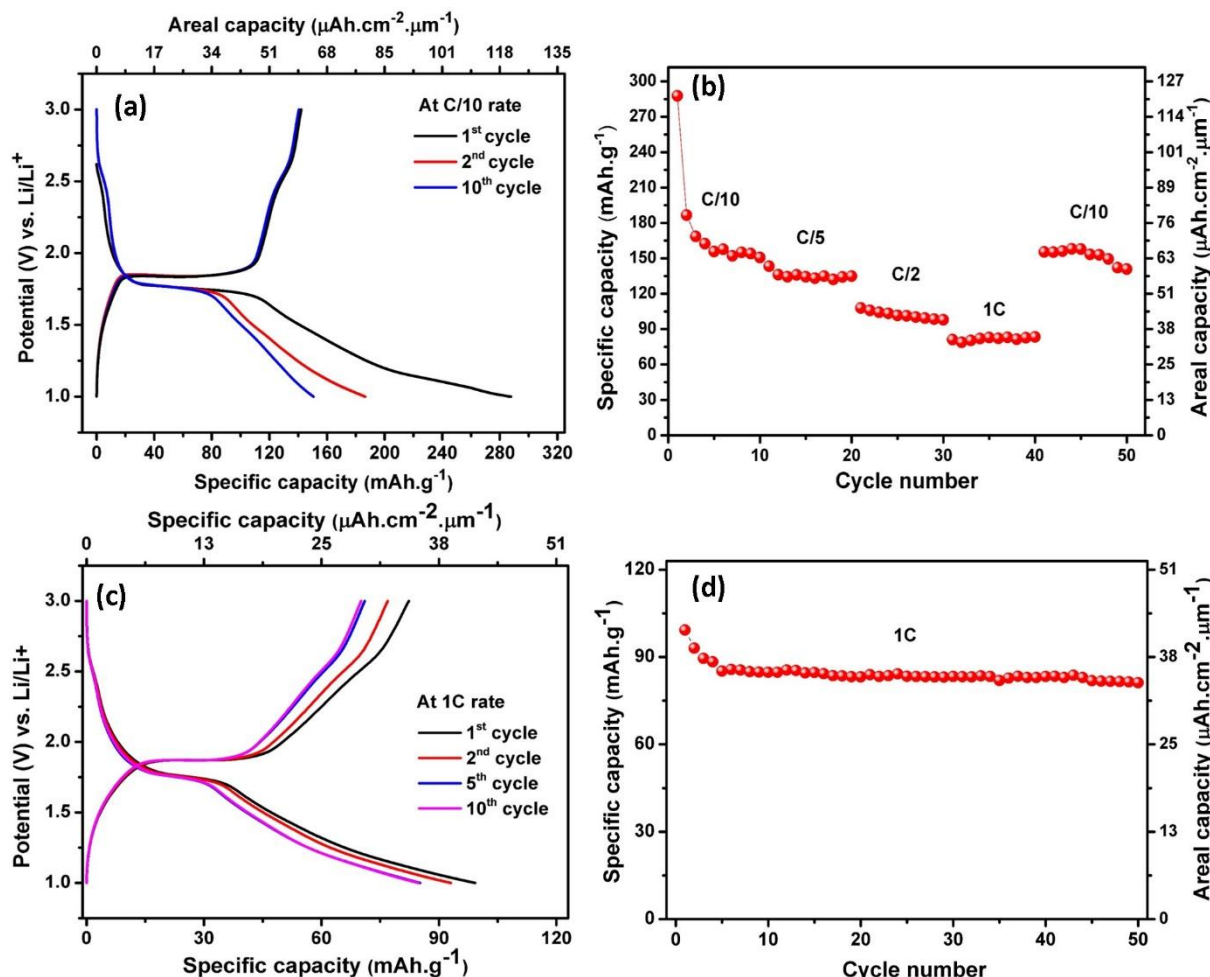
629

630 **Figure 6.** Cyclic voltammograms of anatase TiO₂ NTs on Ti-6Al-4V alloy performed in the
 631 potential range 1-3 V at a scan rate of 0.1 mV.s⁻¹ and 0.5 mV.s⁻¹ (a) and 10 cycles CVs at scan
 632 rate of 0.1 mV.s⁻¹(b).

633

634

635



636

637 **Figure 7.** Charge-discharge profile of anatase TiO₂ NTs on Ti-6Al-4V alloy at C/10 rate (a)
 638 and the discharge capacity vs. cycle number at multiple C-rates (b).

639

640